

# Scalable Blade Coating: A Technique Accelerating the Commercialization of Perovskite-Based Photovoltaics

Jian Cheng, Fan Liu, Zhengqiang Tang, and Yuelong Li\*

Since the first report in 2009 with a power conversion efficiency (PCE) of 3.8%, perovskite solar cells (PSCs) have become the hot research topic in the field of photovoltaics and rapidly achieved a certified PCE of 25.5% within just a decade. Compared to its counterparts such as single-crystalline silicon solar cells or CIGS, PSCs present the obvious advantages of low cost and solution processability. However, the most efficient PSCs are mainly based on devices with an active area of less than  $0.1 \text{ cm}^2$  by a conventional spin-coating method in the lab. To put forward the commercialization of PSCs, it is mandatorily required to manufacture a large-scale PSC module with practical and scalable fabrication techniques. As one of the most viable and promising scalable techniques, the blade coating process with various types available (including doctor-blade coating, slot-die coating, roller coating) has been widely investigated due to many attractive merits of high PCE, easy operation, low cost with cheap facilities, and high materials utilization ratio. Herein, the challenges of fabricating large-area PSCs and manipulation of film quality for highly efficient PSCs fabricated with blade coating are introduced and discussed.

by further solving the issues of improving stability and fabricating large-area modules. However, the current methods of preparing perovskite devices in the laboratories are mainly based on the spin-coating technique, which is a commonly used method for small-area devices but not practical to scale up the active area of devices, although some researchers have obtained a high PCE of 17.82% under the aperture area of  $56.64 \text{ cm}^2$  by control of the antisolvent dripping process during spin coating.<sup>[3]</sup> However, the discontinuous production procedure and low materials utilization ratio<sup>[4]</sup> (only  $\approx 2\%$ ) disable the spin-coating method as a suitable technique for the manufacture of large-scale devices in the mass production status. Currently, several methods to prepare large-area PSCs have been proposed such as blade coating,<sup>[5–9]</sup> screen printing,<sup>[10–14]</sup> inkjet printing,<sup>[15–19]</sup> vapor deposition,<sup>[20–23]</sup> and the soft-template method.<sup>[24,25]</sup>

## 1. Introduction

Until now, the certified record efficiency of single-junction perovskite solar cells (PSCs) has reached 25.5%, which is close to the record efficiency of 26.6% for monocrystalline silicon solar cells.<sup>[1]</sup> At the same time, its material and manufacturing costs are about half compared with silicon solar cells.<sup>[2]</sup> The research community and industrial partners are looking forward to speeding up the commercialization of perovskite-based photovoltaics

Figure 1A compares the performance and shows the annual PCE record of devices prepared by diverse scalable techniques. Among them, the blade coating method is considered as the most promising and viable for future manufacturing modules due to the following factors. First of all, the blade coating method is easy to operate for continuous production, which is critical for mass production during the commercialization process; Second, the materials utilization ratio during blade coating is as high as 80%, which significantly saves the cost of production, especially the cost of expensive charge transporting materials, and minimizes the amount of wastes to the environments; the last will be that the devices prepared by the blade coating method achieve the highest PCE based on the current know-how. Therefore, this method has been most widely studied and this Review will mainly focus on large-area PSCs by blade coating. Figure 1B and Table 1 show the progress of PCEs based on the doctor blade method.

Blade coating is a relatively mature method of manufacturing films.<sup>[26]</sup> Razza et al. prepared PSCs using a two-step method of scrape coating and achieved a PCE of 10.4% with an area of  $10 \text{ cm}^2$  but only 4.3% with the area of  $100 \text{ cm}^2$ .<sup>[27]</sup> This clearly demonstrates that the PCE reduction phenomenon is serious during scaling up the device area of PSCs. There are several reasons for this kind of decay; first of all, the sheet resistance ( $R_{sh}$ ) of the currently used transparent conducting substrate is relatively high, which contributes to the electrical loss of large-area devices, especially the fill factor (FF). Second, the quality of perovskite

J. Cheng, F. Liu, Prof. Y. Li  
Institute of Photoelectronic Thin Film Devices and Technology  
of Nankai University  
Solar Energy Research Center of Nankai University  
Key Laboratory of Photoelectronic Thin Film Devices and  
Technology of Tianjin  
Engineering Research Center of Thin Film Photoelectronic Technology  
Ministry of Education  
Nankai University  
#38 Tongyan Road, Jinnan District, Tianjin 300350, China  
E-mail: lyl@nankai.edu.cn

F. Liu, Prof. Z. Tang  
College of Mechanical Engineering  
Guizhou University  
Huaxi Road South, Huaxi District, Guiyang 550025, China

The ORCID identification number(s) for the author(s) of this article can be found under <https://doi.org/10.1002/ente.202100204>.

DOI: 10.1002/ente.202100204

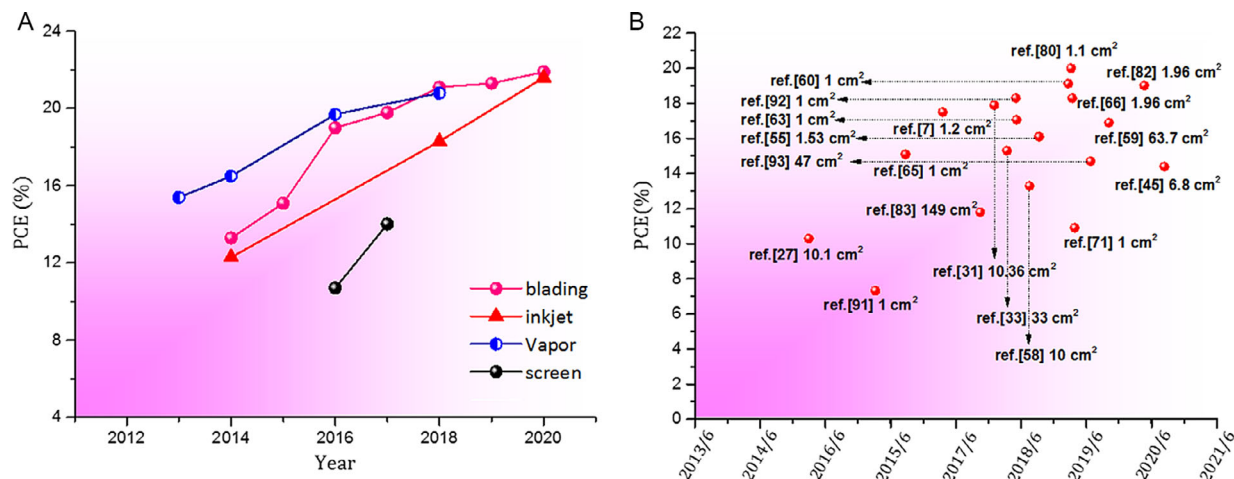


**Figure 1.** A) PCE records of four types of scalable coating methods of PSCs per year.<sup>[6,9,10,12,14,15,18–20,23,51,59,90–94,104]</sup> B) The progress of PCE based on the doctor blade method.<sup>[7,27,31,33,45,55,58–60,63,65,66,71,80–83,90–92]</sup>

film is not well manipulated when the area is up to 100 cm<sup>2</sup>, where many defects including pinholes, coffee rings, and uniformity cause the failure of devices such as short circuit or recombination for less  $V_{oc}$  and  $J_{sc}$ . To eliminate the resistance loss caused during increasing area, researchers have to divide large-area devices into several small strips with centimeter width or deposit metal grid as the highway of charge carrier collection to reduce the resistance loss. In addition, additive engineering can assist blade coating to obtain a uniform and dense perovskite film of higher quality, and passivation engineering can further heal the surface and interfacial defects for less nonradiative recombination and thus enhance the performance of PSCs. In addition to blade coating of the perovskite layer, this process also demonstrates good compatibility in the preparation of other functional layers of the PSCs such as electron or hole transporting layers. In summary, we will first discuss the challenges toward large-area PSCs and the corresponding approaches. Second, the quality control of each functional layer of the device is also summarized in detail.

## 2. Challenges for Large-Area Devices

Although a PCE of 21.9% has been achieved with small-area PSCs by doctor blading,<sup>[9]</sup> increasing the device area will result in a serious reduction in PCE. The loss of performance based on large-area PSCs is mainly caused by 1) the increased series resistance ( $R_s$ ) caused by the transparent conductive oxide (TCO); 2) recombination caused by nonradiative defects within uneven perovskite films such as pinholes and uncoordinated ions; and 3) the lower shunt resistance ( $R_{SH}$ ) by the current leakage. To tackle the challenges of large-area production, there are usually two methods. 1) The entire large-area device is divided into several units with small area or strips and then connected serially through a circuit. This is also a commonly used method, 2) embedding a metal grid between TCO and electron transport layer (ETL) to reduce lateral resistance. The main purpose of these two methods is to reduce the  $R_s$  of large-area devices.

### 2.1. Strategy 1: Modules

For fabricating a module, the devices are normally physically divided into small strips, which are then series interconnected, as shown in Figure 2A. Compared with a single device, it reduces the electrical loss during the carrier transport process and increases the voltage output. Usually, laser scribing is used to create the partitions for interconnections. The scribed parts as the dead area contribute none to the power output of module, which should be reduced to the minimum, and also limit the theoretical geometric fill factor (GFF) to  $\approx 90\%$ .<sup>[28]</sup> Therefore, the optimization of GFF can be mainly achieved by reducing resistance while increasing the active area. The laser scribing process is generally divided into three steps: P1, to remove TCO; P2, to remove the active layer and ETL (by 532 nm laser); and P3, to divide the entire device into subcells (Figure 2A). Palma et al.<sup>[29]</sup> delicately optimized each laser etching step and finally reached 95% GFF. Theoretically, in the traditional P2 scribing process of the n-i-p structure, the ETL should be removed completely to make perfect contact of metal electrode with TCO; however, because the traditional laser scribing of ETL will simultaneously destruct TCO due to similar composition, the ETL cannot be selectively and completely eliminated.<sup>[30]</sup> Consequently, the parasitic resistance of the device is significantly higher.

To deal with this obstacle, Palma et al. compared two types of lasers with a wavelength of 355 and 1064 nm and found that FTO and TiO<sub>2</sub> have similar absorption to the near-IR laser, whereas the absorption coefficient of 355 nm laser of TiO<sub>2</sub> is 2.5 times higher than that of TCO, which could burn out the TiO<sub>2</sub> layer selectively.<sup>[29]</sup> Yang et al. reduced the thickness of TiO<sub>2</sub> from 100 to 10 nm to form the ohmic interconnection contact (FTO/TiO<sub>2</sub>/Au) without causing significant shunts to decrease, as a result, fill factor (FF), the most affected photovoltaic parameter by the  $R_s$ , improved significantly from 0.465 to 0.720 and the PCE increased from 9.42% to 15.14% as well.<sup>[31]</sup> By selecting a better laser technique, Higuchi et al. used the THG-YAG laser (photon energy of 3.49 eV), whose energy is

**Table 1.** Research summary of PSCs prepared by the blade coating method.

Structure of devices	Additives/auxiliary	Methods	PCE [%]	Area [cm <sup>2</sup> ]	Ref.
FTO/TiO <sub>2</sub> /MAPbI <sub>3</sub> /Spiro/Au	–	Slot die	7.01 <sup>a)</sup>	0.09	[95]
ITO/M-PEDOT: PSS/MAPbI <sub>3</sub> Cl <sub>3-x</sub> /PCBM/Ca/Al	–	Doctor blade	10.15 <sup>a)</sup>	0.035	[96]
ITO/PEDOT: PSS/MAPbI <sub>3</sub> Cl <sub>3-x</sub> /PCBM/C60/Ag	–	Doctor blade	10.44	0.1	[97]
ITO/PEDOT: PSS/MAPbI <sub>3</sub> Cl <sub>3-x</sub> /PCBM/Bis-C60/Ag	1,8-diiodooctane	Doctor blade	12.21	0.0314	[5]
ITO/PEDOT: PSS/MAPbI <sub>3</sub> /PCBM/Ag	Humidity assisted	Bar coating	13.03 <sup>a)</sup>	0.021	[98]
ITO/SnO <sub>2</sub> /CsFAPbI <sub>3</sub> Br <sub>3-x</sub> /Spiro/Au	2-Butoxyethanol	Slot die	13.9 <sup>a)</sup>	0.04	[99]
ITO/TiO <sub>2</sub> /MAPbI <sub>3</sub> Cl <sub>3-x</sub> /Spiro/Au	–	Slot die	16.8, 11.1 <sup>a)</sup>	0.09, 168	[82]
ITO/PEDOT: PSS/MAPbI <sub>3</sub> Cl <sub>3-x</sub> /PCBM/Ag	Heat assisted	Roller coating	2.90%	0.12	[100]
ITO/PEDOT: PSS/MAPbI <sub>3</sub> /PCBM/Ag	Heat assisted, humidity assisted	Doctor blade	11.29	0.09	[7]
ITO/PEDOT: PSS/MAPbI <sub>3</sub> /C60/BCP/Al	Heat assisted	Doctor blade	15.10	N/R	[50]
ITO/SnO <sub>2</sub> /MAPbI <sub>3</sub> Cl <sub>3-x</sub> /Spiro/Au	MAAC/heat assisted	Grooved roller coating	15.26	0.1	[4]
ITO/PEDOT: PSS/MAPbI <sub>3</sub> /C60/BCP/Al	PbAc <sub>2</sub> ·3H <sub>2</sub> O as Pb source/heat assisted	Doctor blade	16.40	0.1	[101]
FTO/TiO <sub>2</sub> /MAPbI <sub>3</sub> /Spiro/Au	Heat assisted, rotating magnetic	Roller coating	17.50	0.11	[102]
FTO/TiO <sub>2</sub> /MAPbI <sub>3</sub> /Spiro/Au	Heat assisted	Doctor blade	17.53	0.09	[49]
ITO/PTAA/FAMAPbI <sub>3</sub> /PCBM/C60/BCP/Cu	Heat assisted	Doctor blade	18.00 <sup>a)</sup>	N/R	[103]
FTO/TiO <sub>2</sub> /MAPbI <sub>3</sub> /Spiro/Au	Heat assisted	Doctor blade	18, 16.1	0.11, 1.53	[53]
FTO/TiO <sub>2</sub> Dense/MAPbI <sub>3</sub> /Spiro/Au	Heat assisted	Doctor blade	18.74, 17.06	0.09, 1	[62]
ITO/PTAA/MAPbI <sub>3</sub> /C60/BCP/Al	Heat assisted	Doctor blade	19.00 <sup>a)</sup>	0.08	[6]
ITO/PTAA/CsFAMAPbI <sub>3</sub> Br <sub>3-x</sub> /C60/BCP/Cu	Heat assisted	Doctor blade	19.30 <sup>a)</sup>	N/R	[104]
FTO/TiO <sub>2</sub> /FAMAPbI <sub>3</sub> Br <sub>3-x</sub> /PTAA/Ag	Heat assisted	Doctor blade	19.8 <sup>a)</sup>	0.1	[105]
ITO/MAPbI <sub>3</sub> /C60/BCP/Cu	Methylammonium Hypophosphite (MHP), MACI/Heat assisted	Doctor blade	20.2 <sup>a)</sup>	0.08	[106]
ITO/PTAA/MAPbI <sub>3</sub> /C60/BCP/Cu	l-α-phosphatidylcholine (LP)/Heat assisted	Doctor blade	20.3, 15.3	0.075, 33	[33]
ITO/PTAA/MAPbI <sub>3</sub> /C60/BCP/Cu	LP, cysteine hydrochloride, ACN, MA, MeOH	Slot die	20.8, 14.4	0.1, 6.8	[43]
ITO/PTAA/FA <sub>0.85</sub> MA <sub>0.15</sub> Pb(Br <sub>0.15</sub> I <sub>0.85</sub> ) <sub>3</sub> /C60/BCP/Cu	3-(decyldimethylammonio)-propane sulfonate inner salt/heat assisted	Doctor blade	21.1, 18.3	0.08, 1	[91]
ITO/PTAA/MAPbI <sub>3</sub> /C60/BCP/Cu	LP, MHP, and 1,3-diaminopropane (DAP)/heat assisted	Doctor blade	21.7, 20	0.08, 1.1	[79]
ITO/PTAA/Rb <sub>0.025</sub> Cs <sub>0.025</sub> FA <sub>0.70</sub> MA <sub>0.25</sub> PbI <sub>3</sub> /C60/BCP/Cu	MHP, LP, DAP, CdI <sub>2</sub> /heat assisted	Doctor blade	21.9	0.08	[9]
FTO/TiO <sub>2</sub> /MAPbI <sub>3</sub> Cl <sub>3-x</sub> /Spiro/Ag	Air flow assisted	Slot die	8.1 <sup>a)</sup>	0.0625	[107]
ITO/PEDOT: PSS/MAPbI <sub>3</sub> /PCBM/BCP/Ag	Air flow assisted	Slot die	9.38	0.15	[108]
ITO/PTAA/MAPbI <sub>3</sub> /C60/BCP/Al	Heat, N <sub>2</sub> flow assisted	Doctor blade	12.20	N/R	[51]
ITO/ZnO/MAPbI <sub>3</sub> /Bifluo/MoO <sub>3</sub> /Ag	Heat, N <sub>2</sub> flow assisted	Slot die	12.73	0.067	[109]
ITO/PEDOT: PSS/MaPbI <sub>3</sub> Cl <sub>3-x</sub> /C60/PCBM/BCP/Ag	Heat, N <sub>2</sub> flow assisted	Slot die	13.3, 8.3	0.01, 10	[57]
ITO/SnO <sub>2</sub> /MAPbI <sub>3</sub> /Spiro/Au	N <sub>2</sub> flow assisted	Fully air blade	20.8, 19.12	0.09, 1	[59]
ITO/PTAA/MAPbI <sub>3</sub> /C60/BCP/Cu	LP, MHP and DAP/air flow assisted	Doctor blade	21.3, 16.9	0.08, 63.7	[58]
ITO/SnO <sub>2</sub> /MAPbI <sub>3</sub> Cl <sub>3-x</sub> /Spiro/Au	NMP, MACI	Slot die	18	0.06	[86]
FTO/TiO <sub>2</sub> Dense/MA <sub>0.7</sub> FA <sub>0.3</sub> PbI <sub>3</sub> /Spiro/Au	NMP	Doctor blade	18.96, 15.6 <sup>a)</sup>	0.12, 10.36	[31]
FTO/ZnO/MAPbI <sub>3</sub> /Carbon	Vacuum assisted	Slot die	15.1, 10.6	1, 17.6	[64]
FTO/TiO <sub>2</sub> Dense/MAPbI <sub>3</sub> /Co (II)- and Co (III)-based porphyrins/Au	ZnP/Vacuum assisted	Doctor blade	20.5, 18.3	0.1, 1.96	[65]
FTO/TiO <sub>2</sub> Dense/TiO <sub>2</sub> mesoporous/MAPbI <sub>3</sub> /Spiro/Au	ZnP/Vacuum assisted	Doctor blade	20.0, 19.01	0.1, 1.96	[81]
ITO/PEDOT: PSS/MAPbI <sub>3</sub> /PCBM/BCP/Ag	–	Sequential roller coating	7.36	0.0725	[110]
TiO <sub>2</sub> /MAPbI <sub>3</sub> /Spiro/Au/Pt	Air flow assisted	Blade PbI <sub>2</sub> and soak MAI	11.90	N/R	[69]
ITO/ZnO/MAPbI <sub>3</sub> /P3HT/Ag	–	Sequential slot die	11.96	0.1	[14]
FTO/TiO <sub>2</sub> Dense/TiO <sub>2</sub> mesoporous/MAPbI <sub>3</sub> /Spiro/Au	Air flow assisted	Blade PbI <sub>2</sub> and soak MAI	13.3, 4.3	0.1, 100	[27]

**Table 1.** Continued.

Structure of devices	Additives/auxiliary	Methods	PCE [%]	Area [cm <sup>2</sup> ]	Ref.
ITO/ZnO/MAPbI <sub>3</sub> /BiFuo/Ag	–	Slot die PbI <sub>2</sub> and soak MAI	14.75	0.1	[85]
ITO/NiO <sub>x</sub> /MAPbI <sub>3</sub> /PCBM/BCP/Ag	Vacuum assisted	Sequential doctor blade	16.71, 10.91	0.09, 1	[70]
FTO/TiO <sub>2</sub> Dense/MAPbI <sub>3</sub> Cl <sub>3-x</sub> /Spiro/Au	MAI, NMP	Blade PbI <sub>2</sub> and soak MAI	19.05 <sup>a</sup> , 17.5 <sup>a</sup>	0.12, 1.2	[8]

<sup>a</sup>) Research works based on different processing conditions are separated by gray and white background based on Section 3.1, Processing Conditions.

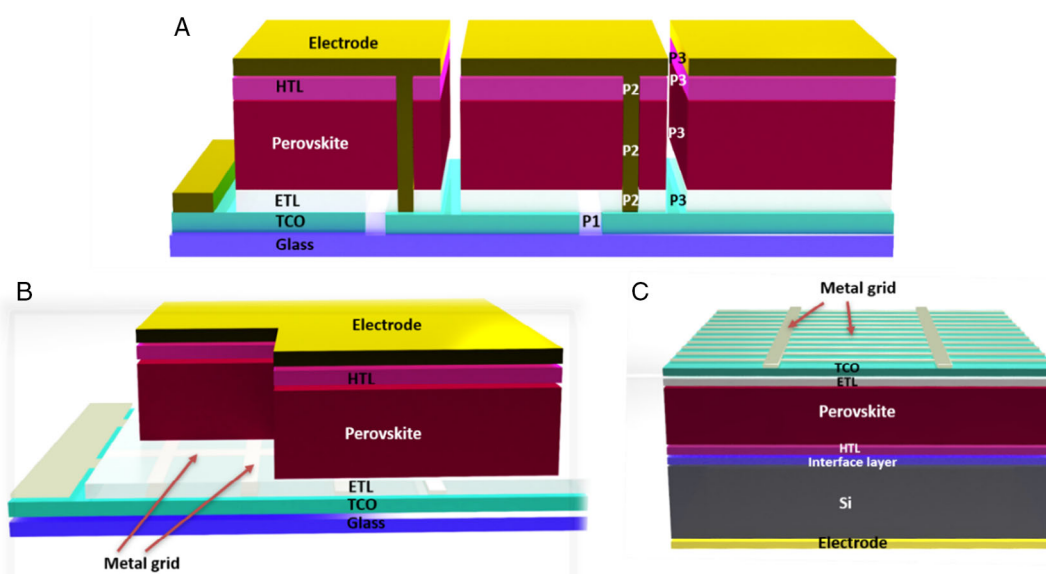


**Figure 2.** Schematic diagram of the typical architectures of three large-area devices. A) Module architecture of PSCs. B) The architecture of PSCs with metal grids. C) Tandem structure of perovskite/single-crystalline silicon solar cells with top metal grid.

intermediate between the bandgaps of TiO<sub>2</sub> (3.2 eV) and FTO (3.57 eV), to selectively eliminate the TiO<sub>2</sub> layer. Taking advantage of this precise laser process, the series resistance of the module was reduced from 0.26 to 0.1  $\Omega \text{ cm}^{-2}$  with increased FF from 0.546 to 0.692 and PCE from 9.42% to 12.6% with an aperture area of 354.45 cm<sup>2</sup>.<sup>[32]</sup> However, in the p–i–n structure, the P2 process has to remove the organic hole transport layers (HTLs).<sup>[33]</sup> Although the way of module effectively reduces the energy loss caused by large area, the dead area from the laser scribing process in the module will give rise to the PCE loss. Three laser partition processes require accurate and expensive laser equipment, which absolutely increases the fabrication cost and complicates the fabrication process.<sup>[34]</sup>

## 2.2. Strategy 2: Metal Grid

Another strategy to enhance the PCE is to insert a metal grid under the ETL, as shown in Figure 2B. Within a TCO/metal grid/ETL device, electrons migrate through ETL and then are collected by TCO and the metal grid sequentially and eventually transferred to the electrode. Compared with the normal TCO/ETL device, the metal grid can effectively reduce electrical loss.<sup>[35]</sup> Research on grid optimization has been widely reported over the past 50 years<sup>[36]</sup> in the field of silicon and thin-film solar cell.<sup>[37,38]</sup>

Wilkinson et al. explored the limits of minimodule and determined the optimal structure of metal grid in PSCs.<sup>[34]</sup> Via calculations based on a small-area PSC with a bandgap of 1.48 eV, the PCE can reach 25%. When the area of cells reaches 4 cm<sup>2</sup>, the PCE drops to 19% and less than 5% for a cell with area of 243 cm<sup>2</sup>. By inserting an optimized front metal grid, the potential PCE reaches 21% for a cell with area >200 cm<sup>2</sup>. The calculation results also show that the thickness of the busbar can be increased and the width should be further reduced to improve the performance of large-area PSCs. However, in reality, excessively thick busbars can disrupt the deposition of the following layers.

Kim et al. deposited a 100 nm-thick metal grid on TCO, by optimizing the structure of the grid, and further reduced the  $R_s$  from 56 to 17  $\Omega \text{ cm}^{-2}$  when cell area was 16 cm<sup>2</sup>. The FF increased from 0.32 to 0.59, and the PCE improved from 5.5% to 12% (certified). By further optimizing the grid structure, a PCE of 16.9% was obtained.<sup>[35]</sup> Zhang et al. fabricated ITO/Ag grid/AZO electrode with an extremely low  $R_{sh}$  of about 3.8  $\Omega \text{ cm}^{-2}$ .<sup>[39]</sup> However in the p–i–n structure the metal grid could be corroded by the HTL; therefore, it is necessary to solve the problem of stability while reducing  $R_s$ .<sup>[40,41]</sup> Hamsch et al.<sup>[40]</sup> further utilized an aluminum grid to increase the conductivity of the TCO; at 25 cm<sup>2</sup> aperture area, the PCE of cells reached 6.7%. To avoid the corrosion of the metal grid, a

thin  $\text{Al}_2\text{O}_3$  layer was deposited on the metal grid as a protective layer, which reduces the probability of short circuit.

### 2.3. The Challenge of Large-Area Perovskite/Si Tandem Solar Cells

Similar to single-junction perovskite, the decrease in PCE of large-area tandem cells (Figure 2C) relative to small cells is mainly caused by an increase in  $R_s$ . The nonuniformity of the film results in the recombination and thus reduces the FF and the PCE. Therefore, one of the efficient strategies for constructing a high-efficiency tandem cell is to optimize the top electrode grid; in contrast, it is important as well to improve  $R_{SH}$  by optimizing the uniformity of each layer in the top cell. Recently, Sahli et al.<sup>[42]</sup> developed monolithic perovskite/silicon tandem cells with a nanocrystalline silicon (nc-Si:H) recombination layer, the steady efficiencies reached 22.0% and 21.2% for aperture areas of 0.25 and 1.43  $\text{cm}^2$ , respectively. Because the nc-Si:H has low lateral conductivity, shunt paths through the top cell were observed, thus obtaining 18% steady-state efficiency with an aperture area of 12.96  $\text{cm}^2$ . In terms of the perovskite absorber layer, recently, researchers demonstrated the great potential of blade coating technique to fabricate perovskite absorber with high quality even on the textured surface of silicon bottom cells.<sup>[43,44]</sup> Zheng et al.<sup>[45,46]</sup> designed an interface layer-free perovskite/silicon homojunction solar cell and achieved a PCE of 21.0% with  $V_{oc}$  of 1.68 V,  $J_{sc}$  of 16.1  $\text{mA cm}^{-2}$ , and high FF of 78% on 4  $\text{cm}^2$  cell. However, as the area increased to 16  $\text{cm}^2$ , the PCE decreased to 17.6% with  $V_{oc}$  of 1.66 V,  $J_{sc}$  of 15.6  $\text{mA cm}^{-2}$ , and FF of 68%. They attributed the drop to 1) higher  $R_s$  by unoptimized structure and thickness of the metal grid and 2) reduced  $R_{SH}$  from 3042 to 1113  $\Omega \text{ cm}^{-2}$  due to non-uniformity of perovskite absorbers and transport layers causing more recombination. In the same report, Zheng et al. also predicted the potential of a higher tandem PCE with FF of 0.8, resulting from a more accurately designed metal grid (requiring  $R_s$  as low as 2  $\Omega \text{ cm}^{-2}$ ). Two months later, Zheng et al. designed a new metal grid for perovskite/silicon homojunction solar cells and obtained 21.8% steady-state efficiency with FF of 0.78 on the 16  $\text{cm}^2$  device. The deficit to the theoretical voltage decreased from 100 to 35 mV, which is benefited by lower  $R_s$ .<sup>[47]</sup>

In addition to optimizing the layout of the grid structure, the aspect ratio also has to be further optimized to reduce the grid resistances; however, the thicker grid prepared by the evaporation (material utilization ratio is only 9%) method will increase the material cost. To make a thicker grid, Kamino et al.<sup>[48]</sup> prepared a low-temperature silver paste by screen printing the front grid of two-terminal perovskite silicon tandem cells. Based on this grid, tandem cells with an aperture area of 57.4  $\text{cm}^2$  achieved a 22.6% steady-state efficiency. The PCE of cells with small active area (1.43  $\text{cm}^2$ ) was about 23%. Researchers also compared the performance of cells with silver grid by evaporation and screen printing, and they found that screen-printed cells have inferior FF and  $J_{sc}$  compared with cells based on the evaporated silver grid. The decrease in FF is mainly due to the higher contact resistance caused by the low curing temperature (130 °C). The decrease in  $J_{sc}$  was mainly due to the increase in the shadow area of the metal grid from 1.25% by evaporation to 3% by screen

printing. This study confirmed that the efficiency gap between large and small tandem cells can be further erased by reducing the contact resistance between the TCO and the metal grid.

## 3. Manipulation of Film Quality

An increasing number of studies have confirmed that perovskite absorbers with high quality and lower defects play a vital role in improving the performance of PSCs.<sup>[33]</sup> During the preparation of perovskite layer by blade coating, the grain size and uniformity of perovskite films are critically controlled by the solvent evaporation rate, which significantly affects the crystallization kinetics and thermodynamic mechanism of perovskite.<sup>[30]</sup> There are several viable methods of controlling the evaporation rate of the solvent during the blade coating process: heating, gas blowing, and vacuum evaporating.<sup>[46]</sup> At the same time, the extraction of the precursor solvent by the antisolvent is also an effective method, especially for small-scale fabrication. The nonuniformity of layers grown on the hydrophobic surface can be overcome with the help of the proper surfactant. The addition of a passivating agent can passivate defects located on the surface and the grain boundary of the perovskite layers.

### 3.1. Processing Conditions

#### 3.1.1. Heating-Assisted Film Formation

The concentration of the solution, the temperature of the substrate, and the speed of the blade movement in the thermally assisted blade coating have a crucial effect on the quality of the film. During the process of thermally assisted blade coating, needle crystals are inclined to be formed when the temperature is too low, coffee rings are normally generated when the concentration is too low, and pinholes and film discontinuities are created when the coating speed is slow. In one-step blading, slow drying at low temperature leads to the formation of crystalline solvates rich in  $\text{PbI}_2$ , along with the  $\text{PbI}_2$  phase, and then eventually creates needle-like perovskite crystals. At high temperature (above 100 °C), the perovskite crystals nucleate and grow directly within the colloidal ink, then forming compact films.<sup>[49]</sup>

Huang and coworkers<sup>[50]</sup> adjusted the thickness of the perovskite film by changing the concentration of the perovskite precursor and the height of the blading channel. By controlling the substrate temperature during blade coating, it was found that a large-grain perovskite crystal was obtained at an optimal temperature of 125 °C. The PCE of PSCs reached 15.1%. Huang and coworkers<sup>[51]</sup> further studied the process of drying precursor solution and crystallization of perovskite. It was found that a coffee ring can be formed when the precursor concentration was less than 350  $\text{mg mL}^{-1}$ , and each coffee ring will limit the growth of crystals, making the perovskite grains smaller. As a result,  $J_{sc}$  (18.9  $\text{mA cm}^{-2}$ ) and  $V_{oc}$  (0.89 V) were lower than those without a coffee ring ( $J_{sc} = 21.89 \text{ mA cm}^{-2}$ ,  $V_{oc} = 1.05 \text{ V}$ ). Hu et al.<sup>[52]</sup> found that the amplitude of the coffee ring decreased with increasing temperature. The solution first grows outward at the crystal nucleus, and concentric rings are formed with the periodic supersaturation of the solution and intermediate movement. Higher substrate temperature shortens the period of



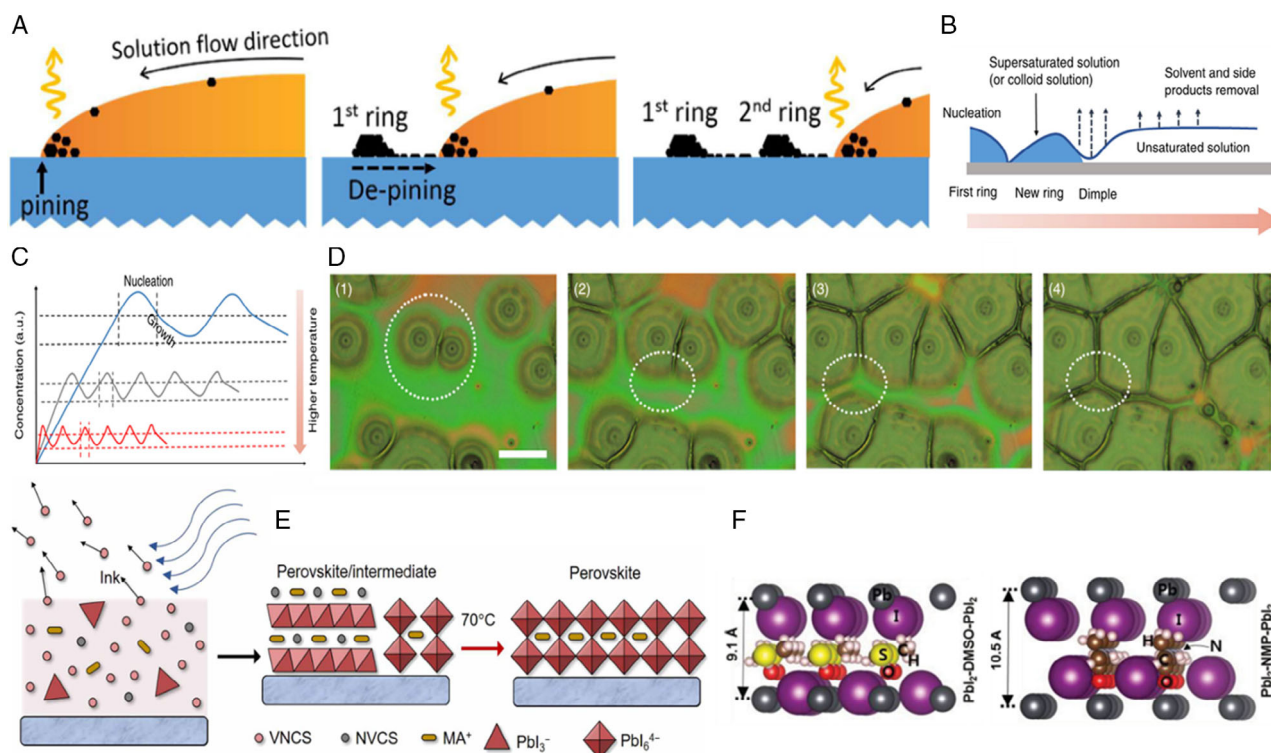


**Figure 3.** A) Schematic diagram of the formation of a coffee ring. Reproduced (Adapted) with permission.<sup>[51]</sup> Copyright 2017, Royal Society of Chemistry. B) The scheme of forming a coffee ring process. C) Periodic relationship between concentration and time of crystallization process at different temperatures. D) In situ micrograph of crystal nucleation and growth at 100 °C. The white scale bar is 50 μm. E) Schematic showing the drying of ink into a perovskite/intermediate film and full crystallization of a perovskite film, volatile noncoordinating solvent (VNCS) and nonvolatile coordinating solvent (NVCS). F) Schematic diagram of the theoretical structure of DMSO and NMP forming intermediate with PbI<sub>2</sub> respectively. Reproduced (Adapted) with permission.<sup>[61]</sup> Copyright 2016, Wiley.

crystal growth and ring formation process (Figure 3). Guerrero and coworkers<sup>[53]</sup> introduced solvent  $\gamma$ -butyrolactone (GBL) and dimethyl sulfoxide (DMSO) to obtain the precursor solution and set the substrate temperature at 150 °C. A coffee ring will appear when the precursor solution is not saturated, and a flat perovskite film will be obtained when the solution is saturated. In the process of heat-assisted engineering, the substrate temperature is limited by the nonvolatile DMF solvent (boiling point of 153 °C). Subbiah et al.<sup>[43]</sup> used the volatile acetonitrile (ACN) combined with methanol and methylamine (MA) to replace the conventional high-boiling-point solvent DMF.<sup>[54]</sup> By replacing the solvent engineering, accelerating the perovskite film-forming dynamic, and then decrease the temperature of substrate from 150 °C to 70 °C.

Liu and coworkers<sup>[52]</sup> analyzed in situ the crystallization mechanism during thermally assisted slot-die coating by taking advantage of in situ microscopic characterization to observe the entire process from nucleation to the formation of polymorphic crystals. The crystal grows from the nucleus to the surroundings, and as the crystal grows, it collides with the adjacent crystal to form a polygonal texture, as shown in Figure 3D. The size and shape of the polygonal crystal are determined by the nucleation density. The higher the nucleation density, the smaller the texture becomes.

The speed of the blade movement during blade coating also has an important influence on the quality and thickness of the film.

Berre et al.<sup>[26,55]</sup> established two mechanistic models depending on blading speed: evaporative (low speed) and Landau–Levich (high speed) models in Figure 4A. The film thickness in Landau–Levich regime increases with the increase in coating speed, whereas the film thickness in the evaporative regime decreases as the coating speed increases. As the solvent continuously evaporates during the film formation process, the mass transfer effect is generated due to solution convection on the moving contact line (Figure 4A).<sup>[56]</sup> In the Landau–Levich regime, the viscosity is no longer ignored, wherein the liquid is dragged out. On the top of the textured c-Si surface, the speed of blading is a key parameter to control the thickness of the perovskite layer shown in Figure 4B. Subbiah et al.<sup>[43]</sup> used the low-temperature slot-die coating method to fabricate a uniform perovskite layer on the textured surface under optimized blading speed (7.5 mm s<sup>-1</sup>) and ink supply rate (400 μL min<sup>-1</sup>).

The film obtained in the Landau–Levich regime is uniform and the density of defects is low, whereas the film obtained in the evaporative regime contains many defects because in an evaporative regime, the wet film takes a longer time to dry due to the presence of the meniscus near the blade. After a long time, the wet film will form a low-energy state but not necessarily a flat film. At higher speed, a liquid film is dragged out by viscous forces and dries afterward (Landau–Levich regime).

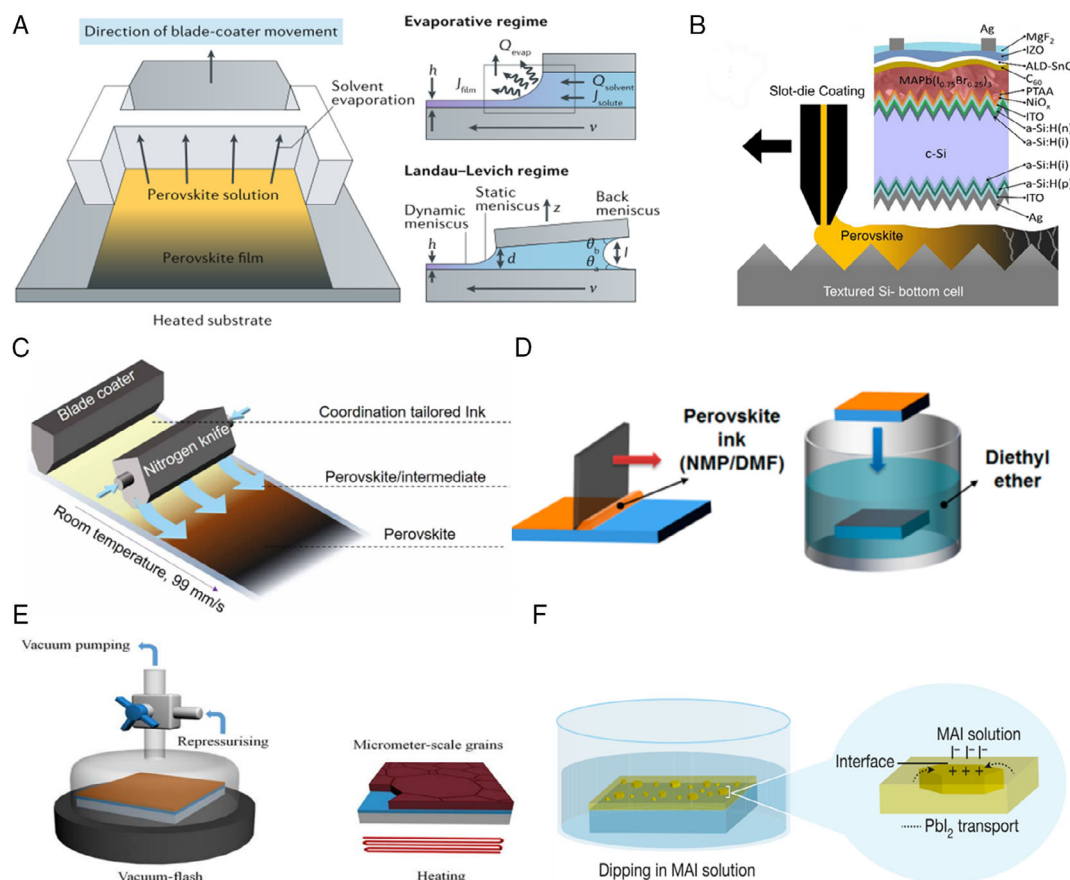


**Figure 4.** Blade coating of perovskite films. A) Left: the blade coating of the film, which forms following evaporation of the solvent, in the Landau–Levich regime. Right: the evaporative and Landau–Levich regimes in more detail (where  $h$  is film thickness,  $v$  is the blade speed,  $Q_{\text{evap}}$  is the flow rate of solvent evaporation,  $Q_{\text{solvent}}$  is the flow rate of solvent entering the box,  $J_{\text{film}}$  is the outward mass flux in the film,  $J_{\text{solute}}$  is the inward mass flux in solution,  $d$  is the meniscus height, and  $\theta_a$ ,  $\theta_b$ , and  $l$  are the contact angle of the liquid surface and the distance of the coater. Reproduced (Adapted) with permission.<sup>[55]</sup> Copyright 2018, Springer Nature. B) Slot-die coating method to fabricate uniform perovskite layer on textured Si bottom cell surface. Reproduced (Adapted) with permission.<sup>[43]</sup> Copyright 2020, American Chemistry Society. C) Schematic illustration for N<sub>2</sub> knife-assisted blade coating of perovskite films. D) Antisolvent (diethyl ether)-assisted doctor blade coating. Reproduced (Adapted) with permission.<sup>[31]</sup> Copyright 2018, American Chemistry Society. E) Vacuum-assisted film formation. Reproduced (Adapted) with permission.<sup>[46]</sup> Copyright 2016, The American Association for the Advancement of Science. F) Schematic diagram of a two-step method. Lead iodide forms perovskite crystal nuclei in an organic salt solution. Reproduced (Adapted) with permission.<sup>[68]</sup> Copyright 2017, Springer Nature.

### 3.1.2. Air-Assisted Film Formation

The use of airflow in the initial stage of film formation after blade coating can accelerate the solvent evaporation of the wet perovskite film (Figure 4C).

Hu et al.<sup>[52]</sup> deposited wet perovskite film by the slot-die coating under a hot nitrogen gun (180 °C under hot air quenching [HAQ]) and accelerated the evaporation rate of the solvent. The researchers compared the difference between the heat-assisted and HAQ method of perovskite film. The perovskite film obtained under the heat-assisted condition has a coffee ring, whereas the film without a coffee ring is formed under HAQ. The roughness of the perovskite formed under HAQ is lower (4.7 nm) than that of heat-assisted ones (38.2 nm). Due to the rapid evaporation of the solvent in the gas-assisted process, the morphology was trapped kinetically, resulting in a smooth film state. Lee et al.<sup>[57]</sup> connected the N<sub>2</sub> gas blower with a slot-die

coater to give an additional quenching effect. The researchers utilized Pb(Ac)<sub>2</sub> as the lead source to promote the rapid crystallization of perovskite. However, in Pb(Ac)<sub>2</sub>-only precursor system, the film surface will solidify and block the evaporation of the solvent and volatile byproduct (MAAc) and then generate voids in the film after the byproduct escapes. Meanwhile, a certain percentage of PbCl<sub>2</sub> was added to make a less-volatile b-product than PbAc<sub>2</sub>, which delays the conversion process of precursor solution. In this way, a complete and dense film can be obtained. Huang and coworkers<sup>[58]</sup> used the airflow-assisted method to prepare the record efficiency in 2019 (16.4%, aperture area of 63.7 cm<sup>2</sup>) for large-area blading of PSCs at low temperature. Among the precursors in this study, the volatile solvent facilitates the film formation and DMSO forms an intermediate with the precursor. The gas blading during the coating process allows the volatile solvent to be quickly blown away; at the same time, DMSO, which is not easily volatilized, forms an

intermediate film (Figure 3E). Finally, DMSO is removed by heating at 70 °C to form a perovskite film with high quality.

Ding et al.<sup>[59]</sup> used air blading to deposit ETL, perovskite layers, and HTL. The PCE of fully air-bladed solar cells reached 20.8% with an area of 0.092 cm<sup>2</sup>, which is superior to 17.28% based on spin-coated PSCs. The authors pointed out that the device by air blade has a slower crystallization process and thus can obtain larger crystal grains. The device fabricated by air blading showed lower MAPbI<sub>3</sub> phase crystallinity and higher (MA)<sub>2</sub>[(PbI<sub>3</sub>)<sub>2</sub>PbI<sub>2</sub>]:2DMSO intermediate phase crystallinity, which is beneficial for grain growth. However, in spin coating, a large amount of DMSO was extracted by the antisolvent, resulting in a decreased intermediate ratio.

### 3.1.3. Antisolvent-Assisted Preparation

In the spin-coating method, antisolvent is frequently used to extract excess solvent to form an intermediate; thereafter, a high-quality pinhole-free perovskite film is formed from the intermediate by heating.<sup>[60]</sup> However, the antisolvent processing window is very short, which makes it difficult to be applied during the blade method. Zhu and coworkers<sup>[8]</sup> compared the window times of different solvent components in the precursor. It was found that the window time of the mixed solvent of DMSO (DMSO: DMF = 9:8 v:v) was about 2 min, whereas the window time of the mixed solvent of NMP (NMP: DMF = 9:8 v:v) was about 8 min. The extension of the window period makes it possible to first deposit the film by blade coating and then put the wet film in the antisolvent for treatment (Figure 4D). Compared with DMSO and DMF, NMP has the lowest vapor pressure. In contrast, NMP can form a complex with PbI<sub>2</sub> to form high-quality perovskite films (Figure 3F).<sup>[61]</sup>

Some researchers compared the antisolvent process with thermally assisted blading<sup>[62]</sup> and air-assisted blading. The results showed that compared with the antisolvent process, the heat-assisted process removes the solvent faster and completely suppresses the intermediate, which leads to low-quality perovskite crystal.<sup>[62]</sup> In the comparison between the antisolvent process and the air-assisted method, the intermediate phase obtained by the antisolvent method is lower and the obtained crystal size is smaller.<sup>[59]</sup>

### 3.1.4. Vacuum-Assisted Film Formation

Vacuum-assisted technology (Figure 4E) also aids film formation by rapid solvent evaporation. The mechanism is similar to that of the antisolvent and air-assisted process. Because the formation rate constant of perovskite is too small, crystal growth will be difficult to control. The Lewis base DMSO can form CH<sub>3</sub>NH<sub>3</sub>I·PbI<sub>2</sub>·DMSO adduct with other precursors, which reduces the formation rate constant of perovskite.<sup>[63]</sup> The antisolvent is used to selectively wash away DMF through a nonpolar antisolvent, whereas the gas-assisted and vacuum-assisted process utilizes the difference of boiling point to remove DMF.<sup>[15]</sup> Li et al.<sup>[46]</sup> believes that the antisolvent-assisted spin-coating process will retain residual DMF or GBL solvents. Unfortunately, these residual solvents reduce the glass transition temperature of the perovskite precursor, increase the mobility during thermal annealing, and ultimately lead to uncontrollable

morphology, and finally result in a wide distribution of perovskite crystal size. However, flash evaporation can increase the glass transition temperature, the viscosity of the precursor, and rapidly form intermediate crystals.

At present, the flash evaporation process is most commonly used in inkjet printing to prepare perovskite layers.<sup>[15,16,19]</sup> Cai et al.<sup>[64]</sup> introduced flash evaporation technology to assist the blade coating method to form a pinhole-free perovskite film and applied it to a large area of carbon-based PSCs and obtained 10.6% PCE with an area of 25 cm<sup>2</sup>. Li et al.<sup>[65]</sup> adopted the flash evaporation technique to assist the blade coating method to deposit the perovskite film. First, the perovskite wet film is prepared by the blade coating method. Second, the substrate is placed in a vacuum chamber of 100 Pa within 30 s, and the solvent is removed for 2 min and finally heated intermediate to form perovskite film. With the aid of monoammonium zinc porphyrin (ZnP) additives, a PCE of 20.05% was obtained. The earlier works demonstrated the potential of flash evaporation-assisted blade coating for the production of pinhole-free and large-area films. However, it can be seen from the experimental process that it faces the same disadvantage as the antisolvent method, that is, the window time for wet film operation is too short. It is also not suitable for the continuous process of roll to roll. However in terms of its excellent performance, this process deserves further exploitation.

### 3.1.5. Sequential Blade Coating

The PSCs prepared by the two-step method of spin coating have comparable performance as the one-step method.<sup>[66]</sup> The growth process in the two-step method is as follows: deposit the PbI<sub>2</sub> layer, and then the MAI molecules in the isopropanol solution diffuse to the interface of the PbI<sub>2</sub> layer and react to form perovskite nucleus, and finally, the nucleus selectively grows to form a MAPbI<sub>3</sub> film, as shown in Figure 4F. The average grain size of perovskite crystals is controlled by two factors: 1) critical energy ( $G_c$ ) and 2) the number of nucleus, as shown in Equation (1).<sup>[67]</sup>

$$Y(\text{grain size}) \propto a \propto \sqrt[3]{\frac{1}{n}} \propto \frac{\Delta G_c}{e^{3kT}} \quad (1)$$

where  $a$  is the length of the cubic edge,  $n$  is nuclei number,  $\Delta G_c$  is critical Gibbs free energy,  $k$  is Boltzmann constant, and  $T$  is thermodynamic temperature.

Some reports have studied the effects of light on the two-step immersion method.<sup>[68]</sup> With the increase in light intensity, the carriers are trapped on the crystal surface, and the surface tension increases. The nucleation density scales logarithmically with light intensity. In the film preparation, the film prepared under 1 sun condition has smaller crystals and higher dense coverage than the film prepared in the dark.

It is also worth noting that the deposition method of MAI, such as immersion of MAI solution, spin coating of MAI solution, etc., has a strong impact on the coverage and decomposition mechanism of the perovskite layer.<sup>[69]</sup>

Guo et al.<sup>[70]</sup> prepared PbI<sub>2</sub> with the blade coating method under the vacuum-assisted condition. The mesoporous structure of PbI<sub>2</sub> is beneficial for the penetration and reaction of MAI. Researchers also found that the deposition temperature of



MAI affected the crystallinity, morphology, and  $\text{PbI}_2$  residues of the perovskite film. When MAI is fabricated by the blade coating method on hot substrate at  $50^\circ\text{C}$ , the device has a PCE of 16.71%. Toshiba Corporation produced a  $703\text{ cm}^2$  flexible device using a two-step blade coating method and achieved a PCE of 11.7%.<sup>[71]</sup> The application potential of the two-step blade coating method on large-area perovskite is strongly proved.

### 3.2. Effect of Additives

Commonly used additives during the formation of perovskite layers include surfactants and passivating agents. On the one hand, surfactants are intentionally used to reduce surface tension and migration of precursor during solvent volatilization and thus improve the flatness of the film. On the other hand, passivation engineering is designed mainly to eliminate nonradiative defects on the grain boundary and the surface of the perovskite film, thereby enhancing the  $V_{\text{oc}}$ ,  $J_{\text{sc}}$ , and FF of the PSCs. There are many types of passivation agents. For related information, refer to the review articles on passivation engineering.<sup>[72–77]</sup> Here we only discuss the effects of several passivation engineering used in the blade coating process.

Huang and coworkers<sup>[33]</sup> monitored the drying process of perovskite solution on the micrometer scale by the in situ method. In the absence of a surfactant (LP), small particles of intermediates are first formed in the solution during the drying process, then the perovskite islands appear, and the small particles of intermediates move to the island. When the intermediates move toward the nearby islands, a gap will be left between the islands, resulting in uneven surface and pinholes in the perovskite film. When the surfactant is added to the solution

(Figure 5A), the surfactant will self-assemble on the surface layer of the solution, thereby reducing the surface tension and then forming a concentration gradient of the surfactant toward the islands, and this gradient forms a Marangoni flow<sup>[78]</sup> from the island to the solution. Marangoni flow interacts with the original flow, thereby suppressing the migration of the intermediate and eventually forming a uniform film, as shown in Figure 5B,C.

In contrast, the problem of wettability is also a major challenge in blade coating, because the deposition of a hydrophilic solution on a hydrophobic surface often causes the solution to shrink, and the perovskite film cannot completely cover the substrate. The pinning effect of the surfactant can “pin” the edge of the solution on the substrate during the entire drying process of the solution. The surfactant (LP)<sup>[9,33,43,58,79]</sup> is an effective and commonly used additive to enhance the solution wettability on a hydrophobic surface. Subbiah et al.<sup>[43]</sup> compared contact angle between DMF-LP, ACN-MeOH, and ACN-MeOH-LP solvent system and hydrophobic PTAA interface. They found that the ACN-MeOH solvent system has a lower contact angle ( $29.7^\circ$ ) than DMF-LP ( $37.9^\circ$ ). While LP surfactant was added into ACN-MeOH system, the contact angle reached minimum ( $21.1^\circ$ ), and the best wettability obtained the best quality of perovskite film. Li et al.<sup>[65]</sup> used ZnP with both surfactant and passivation properties to dope the precursor solution. The characteristics of ZnP molecular surfactants make the perovskite precursor solution completely adhere to the substrate during blade coating. ZnP passivates the grain boundaries and the surface of the perovskite, as shown in Figure 5D, thereby reducing defects and improving the PCE from 18.8% to 20.5%. Tang and coworkers<sup>[80]</sup> demonstrated that the ZnP will form 2D perovskite  $(\text{ZnP})_{0.5}\text{MA}_{n-1}\text{PbI}_{3n+1}$  between the grain boundary of 3D  $\text{MAPbI}_3$  perovskite grains. In this way, ZnP

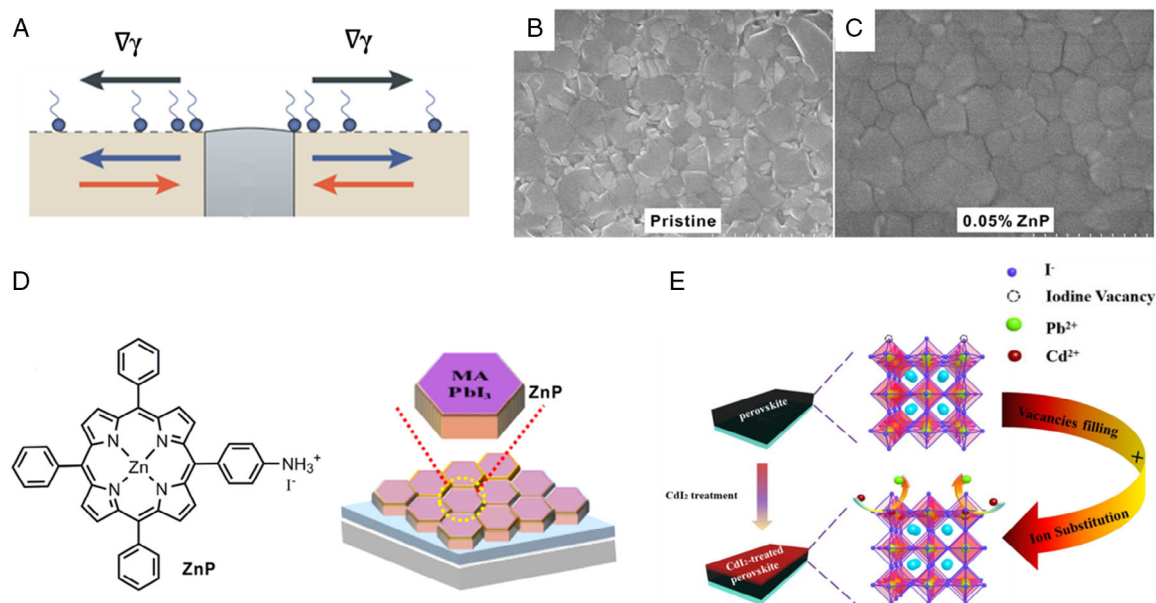


**Figure 5.** A) Schematic illustration of the suppressed solution flow dynamics in the presence of surfactant.  $\nabla\gamma$ , surface tension gradient. Scanning electron microscope (SEM) of perovskite film. Reproduced (Adapted) with permission.<sup>[55]</sup> Copyright 2018, Springer Nature. B) Without ZnP surfactant and C) with ZnP surfactant. Reproduced (Adapted) with permission.<sup>[65]</sup> Copyright 2019, American Chemical Society. D) Schematic diagram of ZnP-passivated  $\text{MAPbI}_3$  surface. Reproduced (Adapted) with permission.<sup>[65]</sup> Copyright 2019, American Chemical Society. E) Schematic illustration of a blade-coated perovskite film with  $\text{CdI}_2$  passivation.

efficiently sutures the grain boundary, which is an effective way to fabricate pinhole-free perovskite film. Tang and coworkers<sup>[81]</sup> also used a vacuum-assisted method to fabricate perovskite film, and ZnP was added and reacted with  $\text{MA}^+$  and  $\text{I}^-$  to yield mono-ammonium zinc porphyrin that is densely bonded on the surface and grain boundary. The function of ZnP effectively removes the pinhole and forms a dense perovskite film. Based on this strategy the best PCE of small-area ( $0.1\text{ cm}^2$ ) PSC reaches 20.0%, and ZnP decreased the energy loss at the perovskite surface and grain boundary, and the large-area ( $1.96\text{ cm}^2$ ) PSC reaches 19.01%. This series of work demonstrated that ZnP is an effective and classic additive to form 2D perovskite and passivate the grain boundary and surface of  $\text{MAPbI}_3$ -based perovskite film. Huang<sup>[79]</sup> used the mechanism that  $-\text{NH}_2$  functional group can coordinate with uncoordinated  $\text{Pb}^{2+}$  ion, and a series of bilateral alkylamine (BAA) was used to passivate the surface and grain boundary of the perovskite layer. High-quality passivation reduced the open-circuit voltage deficit to 0.35 V under AM 1.5G illumination and obtained a  $V_{\text{oc}}$  of 1.18 V. Passivation effectively reduced trap-assisted recombination, leading to FF as high as 0.817. Because  $-\text{NH}_2$  on both sides of the BAA in the grain boundary is coordinated with two grains, the grains are closer together, and finally a pinhole-free perovskite is obtained. The final PCE increased from 18.3% to 21.7%. It is worth noting that BAA passivation was also used to improve the performance of the device in the gas-assisted blade coating of Huang's group,<sup>[58]</sup> indicating that BAA passivation is a viable and effective strategy to improve the performance during blade coating.

Subbiah et al.<sup>[43]</sup> used cysteine hydrochloride to passivate  $\text{MAPbI}_3$  surface, increased the  $V_{\text{oc}}$  by 40 mV, and thus increased PCE to 20.8%. Recently, Huang's group<sup>[9]</sup> combined  $\text{CdI}_2$  and BAA to passivate the surface and grain boundaries of perovskite absorbers.  $\text{Cd}^{2+}$  forms a strong ionic bond  $\text{Cd}-\text{I}$  with I defects in perovskite films, which plays a passivation effect, as shown in Figure 5E, and effectively reduces the interfacial recombination loss. This double-site passivation obtained a minimum voltage loss record of 0.31 V increasing  $V_{\text{oc}}$  to 1.20 V and thus PCE to 21.9%.

### 3.3. Other Functional Layers

In addition to the perovskite layer, other functional layers composed of PSCs such as ETL, HTL, and carbon-based counter electrodes (CE) are also required to be prepared by the blade coating process. Because the blade coating method can prepare a flat film on a large-area device, the material utilization rate is usually high, and the requirements of the solution viscosity are not harsh, and it is also applicable to the roll-to-roll production platform.<sup>[82]</sup>

#### 3.3.1. Charge Transporting Layers

There are few research articles explaining the film-forming mechanism on ETL and HTL but mainly based on the performance comparison between the blade coating method and the spin-coating method. Jung et al.<sup>[83]</sup> deposited poly(3-hexylthiophene) P3HT on the surface of perovskite after passivation by n-hexyl trimethyl ammonium bromide (HTAB) by spin coating and blade

coating. It was found that the best PCEs of large-area devices ( $25\text{ cm}^2$ ) prepared by two methods were both 17.1%.

Giacomo et al.<sup>[82]</sup> prepared devices with  $15.4 \times 15.4\text{ cm}^2$  large area, and prepared the perovskite layer and the Spiro-OMTAD layer by slot die and spin coating, respectively. In terms of performance, the typical  $J-V$  curves of the spin-coated and slot die-coated (Figure 6A) devices are almost identical, as shown in Figure 6B. The researcher divided the large cell into 64 subcells, and it was found in Figure 6C that four consecutive ones were inefficient due to the limitation of spin coating.

Huang et al. fabricated p-i-n devices by blade coating with PTAA as HTL.<sup>[33]</sup> However, when preparing Si/perovskite tandem cells, it is a challenge to prepare a conformally covered PTAA film on the surface of the pyramid structure because thick PTAA accumulates in the valley, whereas there is none or a very thin PTAA layer on the pyramid peak, as shown in Figure 6D. To solve this problem, Huang and coworkers<sup>[44]</sup> combined two methods of nitrogen flow and substrate heating to assist solvent evaporation (Figure 6E) to prepare a uniformly adhered PTAA layer on the textured silicon surface, as shown in Figure 6F.

Ding et al.<sup>[84]</sup> used an air knife to coat the  $\text{SnO}_2$ , perovskite, and spiro layers, and the PCE reached 20.08%. The applicability of air knife coating in the preparation of HTL and ETL was proved. Xin et al.<sup>[4]</sup> prepared a device with  $\text{ITO}/\text{SnO}_2/\text{MAPbI}_3/\text{spiro}/\text{Au}$  structure by roller coating and compared the effects of each layer on device performance by roller coating or spin coating. In the designed series of experiments, the performance of the device prepared by spin coating for all layers reached 15.76%. However, when ETL and HTL layers are coated by roller coating, and the other layers are coated by spin coating, the PCE of the device is reduced by 8.6% and 16.5% compared with the fully spin-coated device, respectively. It shows that the preparation of the spiro-OMeTAD layer by roller coating will greatly affect the performance of the device.

Qin et al.<sup>[85]</sup> believed that the fully symmetrical structure of the spiro-OMeTAD molecule is easy to crystallize and cause an uneven film. Therefore, by preparing Bifluo-OMeTAD molecules that are not easy to crystallize, this molecule exhibits excellent film-forming properties in slot coating.

#### 3.3.2. Counter Electrode

In a single-junction device, CE mainly includes metal electrode and carbon electrode. Metal electrodes are mainly attached to HTL/ETL by evaporation, and some researchers printed silver paste on ETL by screen printing. Schmidt et al.<sup>[86]</sup> applied thermal evaporation and printed CEs to  $\text{ITO}/\text{PEDOT:PSS}/\text{MAPbI}_3/\text{ZnO}/\text{Ag}$  structure devices and compared the performance of the devices. The devices with printed CEs have lower FF and  $J_{\text{sc}}$ . This is due to the decomposition effect of Ag ink on perovskite and its  $\text{ZnO}/\text{Ag}$  interface problems. The carbon electrode is usually deposited on the perovskite layer by blade coating, screen printing, or hot pressing. The main problem of carbon electrodes prepared by blade coating method is limited PCE at 14.9%.<sup>[87]</sup> There are two main reasons: 1) the work function of carbon materials is about 5.0 eV, which does not match with the perovskite layer, resulting in lower performance, and 2) solvent volatilization during the drying of the carbon slurry which causes

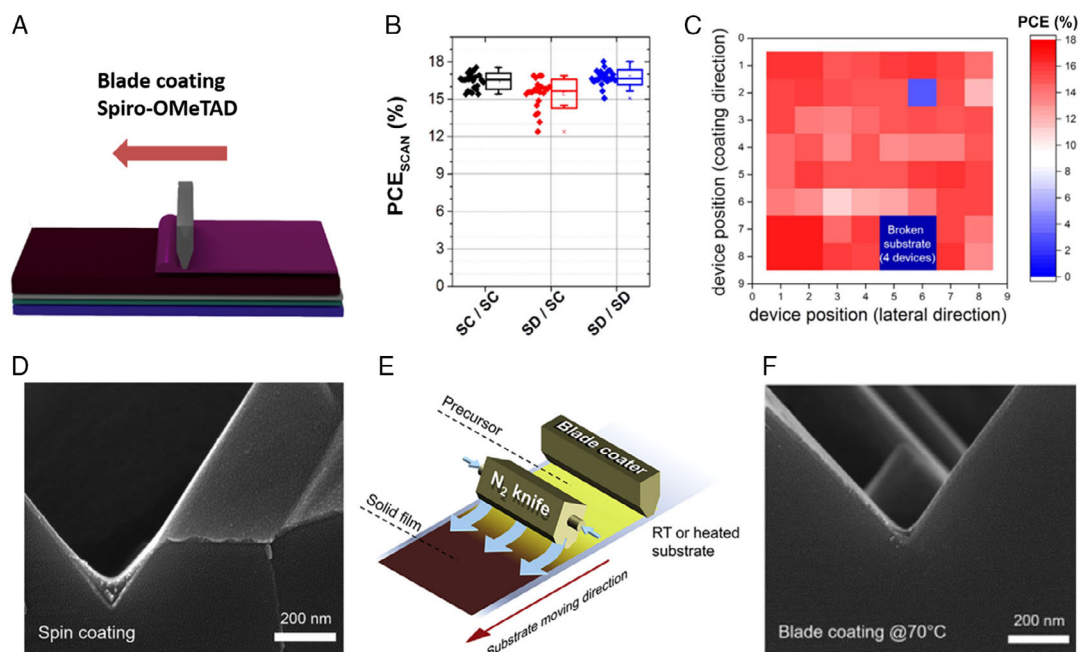


**Figure 6.** A) Schematic illustration of blade coating process of the spiro-OMeTAD layer. Copyright 2018, ELSEVIER. B) The statistical distribution of PCE of the devices, with perovskite/spiro prepared by spin coating/spin coating (SC/SC) and with either one-slot-die-coated/SC (SD/SC) or two-slot-die (SD/SD)-coated layer. Reproduced (Adapted) with permission.<sup>[82]</sup> Copyright 2018, Elsevier. C) PCE mapping of the 64 devices produced on one  $15.4 \times 15.4 \text{ cm}^2$  substrate using slot die coating of perovskite and spin coating of spiro-OMeTAD. Reproduced (Adapted) with permission.<sup>[82]</sup> D) SEM images of PTAA on textured silicon bottom cells deposited by spin coating with the substrate at room temperature. Reproduced with permission.<sup>[44]</sup> Copyright 2020, Elsevier. E) Illustration of N<sub>2</sub>-assisted blade coating. Reproduced (Adapted) with permission. Elsevier. F) N<sub>2</sub>-assisted blade coating with the substrate at 70 °C. Reproduced with permission.<sup>[44]</sup> Copyright 2020, Elsevier.

poor interface contact, resulting in lower FF. To solve the problem of work function mismatch, Wu et al.<sup>[88]</sup> used poly(ethylene oxide) (PEO) to modify the perovskite/carbon material interface. The introduction of PEO forms more upward band bending. Finally, the extraction of holes is promoted. Cheng and coworkers<sup>[89]</sup> improved the contact quality between the carbon layer and perovskite layer; researchers first built a porous carbon aerogel at the interface and then used a grinding process to deal with the carbon electrode, which could effectively reduce the defect on the contact interface.

#### 4. Conclusion and Perspective

This Review introduces the main obstacles in the preparation of large-area devices by the blading method and also summarizes major progress in the preparation of PSCs by the blading method. Large-area devices from blade coating achieved a record of 16.4%<sup>[58]</sup> with the aperture area of  $63.7 \text{ cm}^2$ . However the reduction in PCE caused by area scaling is much higher than the theoretical value.<sup>[30]</sup> In addition to preparing large-area devices by module methods, embedding metal grid between TCO and charge transporting layer is also a promising strategy to scale up the device area. The theoretical GFF in the metal grid strategy is higher than the module strategy, and the process is more concise than the three-step laser scribing method in the module. However, the current application of metal grid in large-area PSCs is very limited due to the fact that it is difficult

to deposit a uniform functional layer on the raised metal lines. In the large-area study of perovskite/Si tandem devices, researchers have found that the reduction of  $R_s$  plays a key role in improving the performance of large-area devices. In the fabrication of grid for tandem devices, the printing method has advantages over the thermal evaporation method, due to the higher material utilization rate of the printing method. The quality of perovskite film determines the performance of large-area devices. This Review scrutinizes the key factors manipulating the quality of film formation in different processes especially for large-area applications. During heat-assisted blade coating, parameters such as substrate temperature, speed of blade coating, and precursor concentration fundamentally determine the quality of perovskite film. In the case of air-assisted blade coating, the solvent can be quickly removed by the airflow, resulting in fast preparation. With regard to the antisolvent process, the operation window time can be extended by addition of Lewis base NMP, which can form strong coordination with PbI<sub>2</sub>. At the same time, proper surfactant in the process of blade coating can inhibit the migration of the intermediate during film formation to obtain a smoother film. The pinning effect of the surfactant can also increase the wettability of the solution on the substrate. Under the optimization of various processes, the small area device based on the blade coating method reached a PCE of over 20% and further to 21.9%, with passivation engineering, which is one of the most effective strategies to further improve the performance by accurately passivating multiple defects with multiple passivating agents.

In addition to the perovskite layer prepared by the blade coating method, other functional layers such as ETL, HTL, and CE can also be prepared by the blade coating method, and the film formation mechanism is simpler than the perovskite active layer, so the application of the blade coating method in these layers has not caused significant performance loss. This Review conveys the confidence in the blading coating technique for promising large-area applications, which will be the key for future commercialization of perovskite-based single- or multijunction photovoltaics.

## Acknowledgements

J.C. and F.L. contributed equally to this work. This work was financially supported by the National Key R&D Program of China (grant no. 2018YFB1500105), the Natural Science Foundation of China (61874167), the Fundamental Research Funds for Central Universities of China and the 111 Project (B16027), the International Cooperation Base (2016D01025), and Tianjin International Joint Research and Development Center.

## Conflict of Interest

The authors declare no conflict of interest.

## Keywords

blade coating, large-area production, material utilization ratios, perovskite solar cells

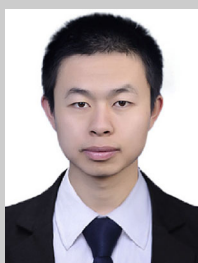
Received: March 18, 2021  
Revised: May 11, 2021  
Published online: July 8, 2021

- [1] K. Yoshikawa, H. Kawasaki, W. Yoshida, T. Irie, K. Konishi, K. Nakano, T. Uto, D. Adachi, M. Kanematsu, H. Uzu, K. Yamamoto, *Nat. Energy* **2017**, 2, 17032.
- [2] L. Meng, J. You, Y. Yang, *Nat. Commun.* **2018**, 9, 5265.
- [3] T. Bu, X. Liu, J. Li, W. Huang, Z. Wu, F. Huang, Y.-B. Cheng, J. Zhong, *Sol. RRL* **2020**, 4, 1900263.
- [4] C. Xin, X. Zhou, F. Hou, Y. Du, W. Huang, B. Shi, C. Wei, Y. Ding, G. Wang, G. Hou, Y. Zhao, Y. Li, X. Zhang, *J. Mater. Chem. A* **2019**, 7, 1870.
- [5] J. H. Kim, S. T. Williams, N. Cho, C.-C. Chueh, A. K. Y. Jen, *Adv. Energy Mater.* **2015**, 5, 1401229.
- [6] Y. Shao, Y. Fang, T. Li, Q. Wang, Q. Dong, Y. Deng, Y. Yuan, H. Wei, M. Wang, A. Gruverman, J. Shield, J. Huang, *Energy Environ. Sci.* **2016**, 9, 1752.
- [7] H. Wu, C. Zhang, K. Ding, L. Wang, Y. Gao, J. Yang, *Org. Electron.* **2017**, 45, 302.
- [8] M. Yang, Z. Li, M. O. Reese, O. G. Reid, D. H. Kim, S. Siol, T. R. Klein, Y. Yan, J. J. Berry, M. F. Van Hest, K. Zhu, *Nat. Energy* **2017**, 2, 17038.
- [9] W. Wu, P. N. Rudd, Z. Ni, C. H. Van Brackle, H. Wei, Q. Wang, B. R. Ecker, Y. Gao, J. Huang, *J. Am. Chem. Soc.* **2020**, 142, 3989.
- [10] A. Priyadarshi, L. J. Haur, P. Murray, D. Fu, S. Kulkarni, G. Xing, T. C. Sum, N. Mathews, S. G. Mhaisalkar, *Energy Environ. Sci.* **2016**, 9, 3687.
- [11] Z. Wan, M. Xu, Z. Fu, D. Li, A. Mei, Y. Hu, Y. Rong, H. Han, *Front. Optoelectron.* **2019**, 12, 344.
- [12] Y. Hu, S. Si, A. Mei, Y. Rong, H. Liu, X. Li, H. Han, *Sol. RRL* **2017**, 1, 1600019.
- [13] F. De Rossi, J. A. Baker, D. Beynon, K. E. A. Hooper, S. M. P. Meroni, D. Williams, Z. Wei, A. Yasin, C. Charbonneau, E. H. Jewell, T. M. Watson, *Adv. Mater. Technol.* **2018**, 3, 1800156.
- [14] K. Hwang, Y. Jung, Y. Heo, F. H. Scholes, S. E. Watkins, J. Subbiah, D. J. Jones, D. Kim, D. Vak, *Adv. Mater.* **2015**, 27, 1241.
- [15] H. Eggers, F. Schackmar, T. Abzieher, Q. Sun, U. Lemmer, Y. Vaynzof, B. S. Richards, G. Hernandez-Sosa, U. W. Paetzold, *Adv. Energy Mater.* **2020**, 10, 1903184.
- [16] T. Abzieher, S. Moghadamzadeh, F. Schackmar, H. Eggers, F. Sutterlüt, A. Farooq, D. Kojda, K. Habicht, R. Schmager, A. Mertens, R. Azmi, L. Klotz, J. A. Schwenzer, M. Hetterich, U. Lemmer, B. S. Richards, M. Powalla, U. W. Paetzold, *Adv. Energy Mater.* **2019**, 9, 1802995.
- [17] C. Liang, P. Li, H. Gu, Y. Zhang, F. Li, Y. Song, G. Shao, N. Mathews, G. Xing, *Sol. RRL* **2018**, 2, 1700217.
- [18] S.-G. Li, K.-J. Jiang, M.-J. Su, X.-P. Cui, J.-H. Huang, Q.-Q. Zhang, X.-Q. Zhou, L.-M. Yang, Y.-L. Song, *J. Mater. Chem. A* **2015**, 3, 9092.
- [19] P. Li, C. Liang, B. Bao, Y. Li, X. Hu, Y. Wang, Y. Zhang, F. Li, G. Shao, Y. Song, *Nano Energy* **2018**, 46, 203.
- [20] C. Momblona, L. Gil-Escrig, E. Bandiello, E. M. Hutter, M. Sessolo, K. Lederer, J. Blochwitz-Nimoth, H. J. Bolink, *Energy Environ. Sci.* **2016**, 9, 3456.
- [21] L. Gil-Escrig, C. Momblona, M.-G. La-Placa, P. P. Boix, M. Sessolo, H. J. Bolink, *Adv. Energy Mater.* **2018**, 8, 1703506.
- [22] D. Forgács, L. Gil-Escrig, D. Pérez-Del-Rey, C. Momblona, J. Werner, B. Niesen, C. Ballif, M. Sessolo, H. J. Bolink, *Adv. Energy Mater.* **2017**, 7, 1602121.
- [23] D. Pérez-Del-Rey, P. P. Boix, M. Sessolo, A. Hadipour, H. J. Bolink, *J. Phys. Chem. Lett.* **2018**, 9, 1041.
- [24] H. Chen, F. Ye, W. Tang, J. He, M. Yin, Y. Wang, F. Xie, E. Bi, X. Yang, M. Gratzel, *Nature* **2017**, 550, 92.
- [25] F. Ye, H. Chen, F. Xie, W. Tang, M. Yin, J. He, E. Bi, Y. Wang, X. Yang, L. Han, *Energy Environ. Sci.* **2016**, 9, 2295.
- [26] M. L. Berre, Y. Chen, D. Baigl, *Langmuir* **2009**, 25, 2554.
- [27] S. Razza, F. Di Giacomo, F. Matteocci, L. Cinà, A. L. Palma, S. Casaluci, P. Cameron, A. D'epifanio, S. Licoccia, A. Reale, T. M. Brown, A. Di Carlo, *J. Power Sources* **2015**, 277, 286.
- [28] S. Moon, J. Yum, L. Löfgren, A. Walter, L. Sansonnens, M. Benkhaira, S. Nicolay, J. Bailat, C. Ballif, *IEEE J. Photovoltaics* **2015**, 5, 1087.
- [29] A. L. Palma, F. Matteocci, A. Agresti, S. Pescetelli, E. Calabro, L. Vesce, S. Christiansen, M. Schmidt, A. D. Carlo, *IEEE J. Photovoltaics* **2017**, 7, 1674.
- [30] P. Wang, Y. Wu, B. Cai, Q. Ma, X. Zheng, W.-H. Zhang, *Adv. Funct. Mater.* **2019**, 29, 1807661.
- [31] M. Yang, D. H. Kim, T. R. Klein, Z. Li, M. O. Reese, B. J. Tremolet De Villers, J. J. Berry, M. F. Van Hest, K. Zhu, *ACS Energy Lett.* **2018**, 3, 322.
- [32] H. Higuchi, T. Negami, *Jpn. J. Appl. Phys.* **2018**, 57, 08RE11.
- [33] Y. Deng, X. Zheng, Y. Bai, Q. Wang, J. Zhao, J. Huang, *Nat. Energy* **2018**, 3, 560.
- [34] B. Wilkinson, N. L. Chang, M. A. Green, A. Hobailie, *Prog. Photovoltaics* **2018**, 26, 659.
- [35] J. Kim, J. S. Yun, Y. Cho, D. S. Lee, B. Wilkinson, A. M. Soufiani, X. Deng, J. Zheng, A. Shi, S. Lim, S. Chen, Z. Hameiri, M. Zhang, C. F. J. Lau, S. Huang, M. A. Green, A. W. Y. Ho-Baillie, *ACS Energy Lett.* **2017**, 2, 1978.
- [36] M. F. Schumann, S. Wiesendanger, J. C. Goldschmidt, B. Benedikt, K. Bittkau, U. W. Paetzold, A. Sprafke, R. B. Wehrspohn, C. Rockstuhl, M. Wegener, *Optica* **2017**, 2, 850.
- [37] Y. Galagan, E. W. C. Coenen, W. J. H. Verhees, R. Andriessen, *J. Mater. Chem. A* **2016**, 4, 5700.



- [38] J. Van Deelen, L. Llerk, M. Barink, *Sol Energy* **2014**, *107*, 135.
- [39] W. Zhang, J. Xiong, W. Sheng, W. E. Liu, J. Li, *J. Power Sources* **2016**, *337*, 118.
- [40] M. Hamsbich, Q. Lin, A. Armin, P. L. Burn, P. Meredith, *J. Mater. Chem.* **2016**, *4*, 13830.
- [41] J. Wang, X. Chen, F. Jiang, Q. Luo, L. Zhang, M. Tan, M. Xie, Y.-Q. Li, Y. Zhou, W. Su, Y. Li, C.-Q. Ma, *Sol. RRL* **2018**, *2*, 1800118.
- [42] F. Sahli, B. A. Kamino, J. Werner, M. Bräuninger, B. Paviet-Salomon, L. Barraud, R. Monnard, J. P. Seif, A. Tomasi, Q. Jeangros, A. Hessler-Wyser, S. De Wolf, M. Despeisse, S. Nicolay, B. Niesen, C. Ballif, *Adv. Energy Mater.* **2018**, *8*, 1701609.
- [43] A. S. Subbiah, F. H. Isikgor, C. T. Howells, M. De Bastiani, J. Liu, E. Aydin, F. Furlan, T. G. Allen, F. Xu, S. Zhumagali, S. Hoogland, E. H. Sargent, I. McCulloch, S. De Wolf, *ACS Energy Lett.* **2020**, *5*, 3034.
- [44] B. Chen, Z. J. Yu, S. Manzoor, S. Wang, W. Weigand, Z. Yu, G. Yang, Z. Ni, X. Dai, Z. C. Holman, J. Huang, *Joule* **2020**, *4*, 850.
- [45] J. Zheng, C. F. J. Lau, H. Mehrvarz, F.-J. Ma, Y. Jiang, X. Deng, A. Soeriyadi, J. Kim, M. Zhang, L. Hu, X. Cui, D. Lee, J. Bing, Y. Cho, C. Chen, M. A. Green, S. Huang, A. W. Y. Ho-Baillie, *Energy Environ. Sci.* **2018**, *11*, 2432.
- [46] X. Li, D. Bi, C. Yi, J.-D. Decoppet, J. Luo, S. M. Zakeeruddin, A. Hagfeldt, M. Grätzel, *Science* **2016**, *353*, 58.
- [47] J. Zheng, H. Mehrvarz, F.-J. Ma, C. F. J. Lau, M. A. Green, S. Huang, A. W. Y. Ho-Baillie, *ACS Energy Lett.* **2018**, *3*, 2299.
- [48] B. A. Kamino, B. Paviet-Salomon, S.-J. Moon, N. Badel, J. Leprat, G. Christmann, A. Walter, A. Faes, L. Ding, J. J. Diaz Leon, A. Paracchino, M. Despeisse, C. Ballif, S. Nicolay, *ACS Appl. Energy Mater.* **2019**, *2*, 3815.
- [49] Y. Zhong, R. Munir, J. Li, M.-C. Tang, M. R. Niazi, D.-M. Smilgies, K. Zhao, A. Amassian, *ACS Energy Lett.* **2018**, *3*, 1078.
- [50] Y. Deng, E. Peng, Y. Shao, Z. Xiao, J. Huang, *Energy Environ. Sci.* **2015**, *8*, 1544.
- [51] Y. Deng, Q. Wang, Y. Yuan, J. Huang, *Mater. Horizons* **2015**, *2*, 578.
- [52] Q. Hu, L. Zhao, J. Wu, K. Gao, D. Luo, Y. Jiang, Z. Zhang, C. Zhu, E. Schaible, A. Hexemer, C. Wang, Y. Liu, W. Zhang, M. Grätzel, F. Liu, T. P. Russell, R. Zhu, Q. Gong, *Nat. Commun.* **2017**, *8*, 15688.
- [53] Z. Bi, X. Rodríguez-Martínez, C. Aranda, E. Pascual-San-José, A. R. Goñi, M. Campoy-Quiles, X. Xu, A. Guerrero, *J. Mater. Chem. A* **2018**, *6*, 19085.
- [54] N. K. Noel, S. N. Habisreutinger, B. Wenger, M. T. Klug, M. T. Horantner, M. B. Johnston, R. J. Nicholas, D. T. Moore, H. J. Snaith, *Energy Environ. Sci.* **2017**, *10*, 145.
- [55] N. Park, K. Zhu, *Nat. Rev. Mater.* **2020**, *1*.
- [56] L. Landau, B. Levich, **1988**, *17*, 141.
- [57] D. Lee, Y.-S. Jung, Y.-J. Heo, S. Lee, K. Hwang, Y.-J. Jeon, J.-E. Kim, J. Park, G. Y. Jung, D.-Y. Kim, *ACS Appl. Mater. Interfaces* **2018**, *10*, 16133.
- [58] Y. Deng, C. H. Van Brackle, X. Dai, J. Zhao, B. Chen, J. Huang, *Sci. Adv.* **2019**, *5*, eaax7537.
- [59] J. Ding, Q. Han, Q. Ge, D. Xue, J. Ma, B. Zhao, Y. Chen, J. Liu, D. B. Mitzi, J. Hu, *Joule* **2019**, *3*, 402.
- [60] N. Ahn, D.-Y. Son, I.-H. Jang, S. M. Kang, M. Choi, N.-G. Park, *J. Am. Chem. Soc.* **2015**, *137*, 8696.
- [61] Y. Jo, K. S. Oh, M. Kim, K.-H. Kim, H. Lee, C.-W. Lee, D. S. Kim, *Adv. Mater. Interfaces* **2016**, *3*, 1500768.
- [62] J. Li, R. Munir, Y. Fan, T. Niu, Y. Liu, Y. Zhong, Z. Yang, Y. Tian, B. Liu, J. Sun, D.-M. Smilgies, S. Thoroddsen, A. Amassian, K. Zhao, S. Liu, *Joule* **2018**, *2*, 1313.
- [63] J.-W. Lee, H.-S. Kim, N.-G. Park, *Acc. Chem. Res.* **2016**, *49*, 311.
- [64] L. Cai, L. Liang, J. Wu, B. Ding, L. Gao, B. Fan, *J. Semicond.* **2017**, *38*, 014006.
- [65] C. Li, J. Yin, R. Chen, X. Lv, X. Feng, Y. Wu, J. Cao, *J. Am. Chem. Soc.* **2019**, *141*, 6345.
- [66] Q. Jiang, Y. Zhao, X. Zhang, X. Yang, Y. Chen, Z. Chu, Q. Ye, X. Li, Z. Yin, J. You, *Nat. Photonics* **2019**, *13*, 460.
- [67] N. Ahn, S. M. Kang, J.-W. Lee, M. Choi, N.-G. Park, *J. Mater. Chem. A* **2015**, *3*, 19901.
- [68] A. Ummadisingu, L. Steier, J.-Y. Seo, T. Matsui, A. Abate, W. Tress, M. Grätzel, *Nature* **2017**, *545*, 208.
- [69] G. Divitini, S. Cacovich, F. Matteocci, L. Cinà, A. Di Carlo, C. Ducati, *Nat. Energy* **2016**, *1*, 15012.
- [70] F. Guo, W. He, S. Qiu, C. Wang, X. Liu, K. Forberich, C. J. Brabec, Y. Mai, *Adv. Funct. Mater.* **2019**, *29*, 1900964.
- [71] T. Corporation, [https://www.nedo.go.jp/english/news/AA5en\\_100391.html](https://www.nedo.go.jp/english/news/AA5en_100391.html), (accessed: 2018).
- [72] B. Chen, P. N. Rudd, S. Yang, Y. Yuan, J. Huang, *Chem. Soc. Rev.* **2019**, *48*, 3842.
- [73] J. M. Ball, A. Petrozza, *Nat. Energy* **2016**, *1*, 16149.
- [74] Z. Ni, C. Bao, Y. Liu, Q. Jiang, W.-Q. Wu, S. Chen, X. Dai, B. Chen, B. Hartweg, Z. Yu, Z. Holman, J. Huang, *Science* **2020**, *367*, 1352.
- [75] F. Gao, Y. Zhao, X. Zhang, J. You, *Adv. Energy Mater.* **2020**, *10*, 1902650.
- [76] W. Qi, X. Zhou, J. Li, J. Cheng, Y. Li, M. J. Ko, Y. Zhao, X. Zhang, *Sci. Bull.* **2020**.
- [77] X. Zhou, W. Qi, J. Li, J. Cheng, Y. Li, J. Luo, M. J. Ko, Y. Li, Y. Zhao, X. Zhang, *Sol. RRL* **2020**, 2000308.
- [78] H. Kim, F. Boulogne, E. Um, I. Jacobi, E. Button, H. Stone, *Phys. Rev. Lett.* **2016**, *116*, 124501.
- [79] W.-Q. Wu, Z. Yang, P. N. Rudd, Y. Shao, X. Dai, H. Wei, J. Zhao, Y. Fang, Q. Wang, Y. Liu, Y. Deng, X. Xiao, Y. Feng, J. Huang, *Sci. Adv.* **2019**, *5*, eaav8925.
- [80] J. Cao, C. Li, X. Lv, X. Feng, R. Meng, Y. Wu, Y. Tang, *J. Am. Chem. Soc.* **2018**, *140*, 11577.
- [81] X.-C. Li, C.-L. Li, Y.-Y. Wu, J. Cao, Y. Tang, *Sci. China Chem.* **2020**, *63*, 777.
- [82] F. Di Giacomo, S. Shanmugam, H. Fledderus, B. J. Bruijns, W. J. H. Verhees, M. S. Dorenkamp, S. C. Veenstra, W. Qiu, R. Gehlhaar, T. Merckx, T. Aernouts, R. Andriessen, Y. Galagan, *Sol. Energy Mater. Sol. Cells* **2018**, *181*, 53.
- [83] E. H. Jung, N. J. Jeon, E. Y. Park, C. S. Moon, T. J. Shin, T.-Y. Yang, J. H. Noh, J. Seo, *Nature* **2019**, *567*, 511.
- [84] J. Ding, Q. Han, Q.-Q. Ge, D.-J. Xue, J.-Y. Ma, B.-Y. Zhao, Y.-X. Chen, J. Liu, D. B. Mitzi, J.-S. Hu, *Joule* **2019**, *3*, 402.
- [85] T. Qin, W. Huang, J.-E. Kim, D. Vak, C. Forsyth, C. R. McNeill, Y.-B. Cheng, *Nano Energy* **2017**, *31*, 210.
- [86] J. B. Whitaker, D. H. Kim, B. W. Larson, F. Zhang, J. J. Berry, M. F. Van Hest, K. Zhu, *Sustainable Energy Fuels* **2018**, *2*, 2442.
- [87] Z. Wu, Z. Liu, Z. Hu, Z. Hawash, L. Qiu, Y. Jiang, L. K. Ono, Y. Qi, *Adv. Mater.* **2019**, *31*, 1804284.
- [88] T. M. Schmidt, T. T. Larsen-Olsen, J. E. Carlé, D. Angmo, F. C. Krebs, *Adv. Energy Mater.* **2015**, *5*, 1500569.
- [89] Y. Xie, J. Cheng, H. Liu, J. Liu, B. Maiti, J. Ma, Y. Qiang, H. Shi, C. Geng, Y. Li, G. Yang, *Carbon* **2019**, *154*, 322.
- [90] A. T. Mallajosyula, K. Fernando, S. Bhatt, A. Singh, B. W. Alphenaar, J.-C. Blancon, W. Nie, G. Gupta, A. D. Mohite, *Appl. Mater. Today* **2016**, *3*, 96.
- [91] X. Zheng, Y. Deng, B. Chen, H. Wei, X. Xiao, Y. Fang, Y. Lin, Z. Yu, Y. Liu, Q. Wang, J. Huang, *Adv. Mater.* **2018**, *30*, 1803428.
- [92] F. Matteocci, L. Vesce, F. Kosasih, L. Castriotta, S. Cacovich, A. L. Palma, G. Divitini, C. Ducati, A. Di Carlo, *ACS Appl. Mater. Interfaces* **2019**, *11*, 25195.
- [93] M. Liu, M. B. Johnston, H. J. Snaith, *Nature* **2013**, *501*, 395.
- [94] Q. Lin, A. Armin, R. C. R. Nagiri, P. L. Burn, P. Meredith, *Nat. Photonics* **2015**, *9*, 106.

- [95] D. Burkitt, J. Searle, T. Watson, *R. Soc. Open Sci.* **2018**, 5, 172158.
- [96] H. Back, J. Kim, G. Kim, T. Kyun Kim, H. Kang, J. Kong, S. Ho Lee, K. Lee, *Sol. Energy Mater. Sol. Cells* **2016**, 144, 309.
- [97] Z. Yang, C.-C. Chueh, F. Zuo, J. H. Kim, P.-W. Liang, A. K. Y. Jen, *Adv. Energy Mater.* **2015**, 5, 1500328.
- [98] J.-W. Lee, S.-I. Na, S.-S. Kim, *J. Power Sources* **2017**, 339, 33.
- [99] Y. Galagan, F. Di Giacomo, H. Gorter, G. Kirchner, I. De Vries, R. Andriessen, P. Groen, *Adv. Energy Mater.* **2018**, 8, 1801935.
- [100] J. A. Ciro Villegas, M. Mejia Escobar, F. Jaramillo, *Sol. Energy* **2017**, 150, 570.
- [101] W. Kong, G. Wang, J. Zheng, H. Hu, H. Chen, Y. Li, M. Hu, X. Zhou, C. Liu, B. N. Chandrashekar, A. Amini, J. Wang, B. Xu, C. Cheng, *Sol. RRL* **2018**, 2, 1700214.
- [102] Y. Lin, X. Ye, Z. Wu, C. Zhang, Y. Zhang, H. Su, J. Yin, J. Li, *J. Mater. Chem. A* **2018**, 6, 3986.
- [103] Y. Deng, Q. Dong, C. Bi, Y. Yuan, J. Huang, *Adv. Energy Mater.* **2016**, 6, 1600372.
- [104] S. Tang, Y. Deng, X. Zheng, Y. Bai, Y. Fang, Q. Dong, H. Wei, J. Huang, *Adv. Energy Mater.* **2017**, 7, 1700302.
- [105] M. He, B. Li, X. Cui, B. Jiang, Y. He, Y. Chen, D. O'neil, P. Szymanski, M. Ei-Sayed, J. Huang, Z. Lin, *Nat. Commun.* **2017**, 8, 16045.
- [106] W. Wu, Q. Wang, Y. Fang, Y. Shao, S. Tang, Y. Deng, H. Lu, Y. Liu, T. Li, Z. Yang, *Nat. Commun.* **2018**, 9, 1625.
- [107] G. Cotella, J. Baker, D. Worsley, F. De Rossi, C. Pleydell-Pearce, M. Carnie, T. Watson, *Sol. Energy Mater. Sol. Cells* **2017**, 159, 362.
- [108] D. Burkitt, P. Greenwood, K. Hooper, D. Richards, V. Stoichkov, D. Beynon, E. Jewell, T. Watson, *MRS Adv.* **2019**, 4, 1399.
- [109] J. E. Kim, Y. S. Jung, Y. J. Heo, K. Hwang, T. Qin, D. Y. Kim, D. Vak, *Sol. Energy Mater. Sol. Cells* **2018**, 179, 80.
- [110] S.-M. Park, Y.-J. Noh, S.-H. Jin, S.-I. Na, *Sol. Energy Mater. Sol. Cells* **2016**, 155, 14.



**Jian Cheng** received his Bachelor degree from Shihezi University in 2015 and received his Master's degree from Xinjiang University in 2019. He is currently a research assistant at Nankai University. His main research focuses on large-scale perovskite solar cells.



**Fan Liu** received his Bachelor's degree from Chongqing Jiaotong University. He is currently a Master's student at Guizhou University and an exchange student at Nankai University. His main research focuses on large-scale perovskite-based tandem solar cells.



**Zhengqiang Tang** is an associate professor at School of Mechanical Engineering, Guizhou University. He received his Ph.D. in Mechanical Engineering from South China University of Technology in 2014. He was a visiting graduate student at University of California, San Diego (UCSD, US), from 2011 to 2013. His research interests are coating design and coating manufacturing, including antiwear and corrosive resistance coating, antibacterial coating, biocompatible coating, etc.



**Yuelong Li** is an associate professor at Nankai University since October 2016. He received his Ph.D. from the Korea Institute of Science and Technology (KIST/UST, Korea) in 2012 and started his postdocs at the University of California-San Diego (UCSD, US) and then the Spanish National Research Council (CSIC, Spain) as the Marie Curie fellow. He stayed at the University of Oxford (2015) and the University of Cambridge (2018) as the visiting scholar. His research mainly focuses on optoelectronic materials and devices such as perovskite solar cells, tandem solar cells, perovskite single crystals, flexible energy electronics, etc.